Geophysical Journal International

Large extensional aftershocks in the continental forearc triggered by the 2010 Maule earthquake, Chile

Journal:	*Geophysical Journal International*
Manuscript ID:	GJI-11-0334.R1
Manuscript Type:	Research Paper
Date Submitted by the Author:	06-Nov-2011
Complete List of Authors:	Ryder, Isabelle; University of Liverpool, School of Environmental Sciences Rietbrock, Andreas; University of Liverpool, School of Environmental Sciences Kelson, Keith; Fugro Consultants, Inc. Burgmann, R.; UC Berkeley, Berkeley Seismological Laboratory Floyd, Michael; Massachusetts Institute of Technology, Department of Earth, Atmospheric and Planetary Sciences Vigny, Christophe; École Normale Supérieure, Département Terre Atmosphère Océan Socquet, Anne; Université Joseph Fourier, Institut des Sciences de la Terre Carrizo, Daniel; Universidad de Chile, Departamento de Geofisica
Keywords:	Creep and deformation < COMPOSITION and PHYSICAL PROPERTIES, Satellite geodesy < GEODESY and GRAVITY, Seismic cycle < GEODESY and GRAVITY, Seismicity and tectonics < SEISMOLOGY, Continental margins: convergent < TECTONOPHYSICS, Kinematics of crustal and mantle deformation < TECTONOPHYSICS, Subduction zone processes < TECTONOPHYSICS

Large extensional aftershocks in the continental forearc triggered by the 2010 Maule earthquake, Chile

Isabelle Ryder[1], Andreas Rietbrock[1], Keith Kelson[2], Roland Bürgmann[3], Michael Floyd[4], Anne Socquet[5], Christophe Vigny[6], Daniel Carrizo[7]

[1]School of Environmental Sciences, University of Liverpool
[2]Fugro Consultants, Inc., Walnut Creek, CA
[3]Berkeley Seismological Laboratory, UC Berkeley, CA
[4]Department of Earth, Atmospheric and Planetary Sciences, Massachusetts Institute of Technology
[5]Département Terre Atmosphère Océan, École Normale Supérieure
[6]Observatoire des Sciences de l'Univers de Grenoble
[7]Department of Geophysics, University of Chile

Abstract

The M_w 8.8 Maule earthquake occurred off the coast of central Chile on 27 February 2010 and was the sixth largest earthquake to be recorded instrumentally. This subduction zone event was followed by thousands of aftershocks both near the plate interface and in the overriding continental crust. Here we report on a pair of large shallow crustal earthquakes that occurred on 11 March 2010 within 15 minutes of each other near the town of Pichilemu, on the coast of the O'Higgins Region of Chile. Field and aerial reconnaissance following the events revealed no distinct surface rupture. **We infer from geodetic data spanning both events that the ruptures occurred on synthetic SW-dipping normal faults. The first, larger rupture was followed by buried slip on a steeper fault in the hanging wall.** The fault locations and geometry of the two events are additionally constrained by locations of aftershock seismicity based on the International Maule Aftershock Dataset (IMAD). The maximum slip on the main fault is about 3 m and, consistent with field results, the onshore slip is close to zero near the surface. Satellite radar data also reveal that significant aseismic afterslip occurred following the two earthquakes. Coulomb stress modelling indicates that the faults **were positively stressed by up to 40 bars** as a result of slip on the subduction interface in the preceding megathrust event; in other words, the Pichilemu earthquakes should be considered aftershocks of the Maule earthquake. **The occurrence of these extensional events suggests that regional interseismic compressive stresses are small.** Several recent large shallow crustal earthquakes in the overriding plate following the 2011 M_w 9.0 Tohoku-Oki earthquake in Japan may be an analogue for the triggering process at Pichilemu.

1. Introduction

The M_w8.8 Maule megathrust event occurred on the subduction zone interface between the down-going Nazca plate and the overriding South American plate, rupturing a length of about 500 km (Fig. 1a). Prior to 2010, this portion of the subduction zone had last ruptured in a major earthquake in 1835, and had been identified as a seismic gap (e.g. Ruegg et al., 2009). During the 2010 rupture, seafloor uplift generated tsunamis that caused significant damage locally and surges up to 2 metres high in New Zealand. Several estimates of slip distribution have been published (Lay et al., 2010, Delouis et al., 2010, Moreno et al., 2010, Tong et al., 2010, Lorito et al., 2011, Pollitz et al., 2011, Vigny et al., 2011), with as much as 20 m of slip on the northern part of the rupture. Using the slip distribution we derived from the Tong et al. (2010) InSAR dataset to forward model surface displacements (see Appendix B), we

find that that the town of Pichilemu at the northern end of the rupture zone (~34.4°S) experienced 4.2 m of WSW horizontal motion and a small amount of uplift (0.3 m).

The density of aftershock activity during the first few months following the Maule earthquake was greatest in the north, in the region of greatest coseismic slip. Thousands of aftershocks occurred near the plate interface, and many also occurred in the shallow crust of the overriding plate (e.g. Fig. 1b). On 11 March 2010, two large aftershocks occurred within 15 minutes of each other near the town of Pichilemu. Damage to buildings was sustained locally, and small tsunami waves were reported offshore. In this paper we use geodetic and seismic data to constrain the location, geometry and slip distribution of the two events (hereafter referred to as Event 1 and Event 2). We also test to what extent these ruptures were promoted by the Maule earthquake.

2. Field investigation following the Pichilemu events

On 12 March 2010, members of the Geotechnical Extreme Events Reconnaissance (GEER) team conducted a field and aerial reconnaissance of the epicentral area to assess the possibility of surface rupture along a shallow crustal fault. The team reviewed pre-earthquake imagery and identified several geomorphic features that could be a result of long-term surface faulting, including a prominent west-facing topographic escarpment extending inland from Playa Puertecillo (Fig. 1b). The review also showed the presence of a flight of Pleistocene marine-terrace surfaces that extend across the up-dip projections of possible SW- or NE-dipping fault planes, and thus provide datums to evaluate possible surface deformation. Ground reconnaissance was completed on 12 March along asphalt highways between the towns of Litueche and Pichilemu (Fig. 1b). Although scarps and other evidence of recent ground deformation were observed, no feature was laterally continuous or consistent with surface rupture associated with the aftershock pattern or transtensional deformation; the features are interpreted to be related to secondary effects from strong ground motion or slope instability.

Aerial reconnaissance of the epicentral area was completed in a small, high-wing aircraft, and included review of the Pichilemu valley, the coastline between southern Pichilemu and the mouth of Rio Rapel (about 70 km of coastline), and the coastal ranges between Litueche and Playa Puertecillo (Fig. 1b). This traverse covered the onshore, up-dip projections of the possible SW-dipping and NE-dipping nodal planes, as well as the coastline and the northwestward projections of the possible nodal planes. No potentially fault-related features were observed on valley floors, across elevated marine terraces, or in coastal sea cliffs. In particular, the escarpment near Playa Puertecillo exhibited no evidence of recent surface deformation; this 180 m-high escarpment is probably related to different rock types, sea-cliff erosion, and/or surface uplift that preceded the 2010 earthquakes. In summary, the ground and aerial reconnaissance efforts observed no evidence of surface rupture related to the 11 March earthquakes.

3. Seismicity

We carried out a preliminary analysis of data from all IMAD stations, which combines data collected by Chilean, US, French, German, and UK seismic stations deployed in the few weeks following the Maule earthquake. We consider data during the time interval 20 March – 2 June, so many of these events will be aftershocks of the two large Pichilemu earthquakes. For the Maule earthquake zone as a whole, more than 30,000 seismic events can be identified based on an association threshold of at least 15 P-wave arrivals (Rietbrock et al., 2010). Because most of the seismicity is located offshore, automatic locations based only on P-wave arrival times have poorly-constrained depth estimates. We therefore used an iterative approach to increase the number of P-wave arrival time picks, to

obtain additional S-wave arrival times, and in the same step to increase the accuracy of the automatic picks. Random manual checks were carried out to optimize the processing parameters. Fig. 1b shows seismicity in the Pichilemu area that occurred during the interval 20 March - 2 June. All of these events have at least 20 and 10 well-constrained arrival times for the P- and S-wave, respectively. The 2D TIPTEQ (Haberland et al., 2009) velocity model (rotated perpendicular to the trench) is used for the final 2D location step. Fig. 2 is a cross-section showing events within 10 km on either side of the lines A-A' and B-B' marked in Fig. 1b. The lines are oriented perpendicular to the strike of the shallow aftershock cluster. The aftershock locations support a southwest-dipping geometry of at least one of the March ruptures. Just below the steeply SW-dipping seismicity cluster a sub-horizontal band of events delineates the subducting Nazca Plate.

The Global CMT (GCMT) locations place the two large Pichilemu earthquakes about two kilometres apart offshore (Fig. 1b), while the NEIC locations place the two events ~10 km to the NE of the linear aftershock cluster. It should be borne in mind that GCMT solutions have location errors of 10-30 km and NEIC solutions have errors of 5-15 km (Weston et al., 2011). **Regarding estimates of source parameters, the first moment tensor solution is likely better constrained than the second, because the latter's wave train will have been overprinted by that from the first event just 15 minutes before.** The GCMT focal mechanism for the first aftershock suggests a nearly pure normal sense of motion on a fault dipping either SW or NE with moderate dip (Fig. 1b). The nodal planes of the GCMT solution for the second event again suggest a normal sense of motion, but with a fault dip that is either very shallow (6°) to the ENE or very steep (86°) to the WSW (Fig. 1b), and outside of the expected dip range for normal faults of 30-60º (Jackson and White, 1989). The GCMT estimate of seismic moment for the first aftershock is 2.39 x 10^{19} N m and 3.49 x 10^{19} N m for the second aftershock, which correspond to moment magnitudes of 6.9 and 7.0 respectively. **The NEIC lists the magnitudes as 6.9 (M_wUCMT) and 6.7 (M_wWCMT). While the magnitude estimates for the first event are consistent, the variation in magnitude estimates for the second event may point to the difficulty in estimating source parameters when waveforms are overprinted.**

4. Geodetic data

4.1 Coseismic interferogram

Coseismic ALOS PALSAR interferograms processed for investigating surface deformation resulting from the Maule earthquake show disturbance of the phase fringes in the Pichilemu area (Fig. A1). This disturbance is attributed to the Pichilemu earthquakes, and suggests deformation on a NW/SE-striking fault. We obtained a better sense of the Pichilemu coseismic signal by processing an ALOS PALSAR pair on Track 114 with start date on 9 March (two days before the earthquakes) and end date on 24 April, i.e. both scenes post-dated the Maule earthquake. The wrapped interferogram shown in Fig. 3a has a long wavelength phase variation along its length, which we interpret as postseismic deformation following the Maule event. There is also a clear local deformation signal in the Pichilemu area, with over 50 cm line-of-sight (LOS) increase to the southwest of a NW/SE-trending line running inland from the coast, and a smaller amount of LOS increase (~12 cm) on the NE side. This displacement pattern is qualitatively consistent with normal faulting on a SW-dipping normal fault, with hanging wall subsidence on the SW side of the fault.

4.2 Postseismic interferogram

Fig. 3b shows a postseismic Envisat IS2 interferogram (descending track 53) for the Pichilemu aftershocks. Because the start date of this interferogram is 26 March and the end date is 4 June 2010, it may again include significant

postseismic signal from the Maule main shock as well as a local postseismic signal of the Pichilemu events. There is a clear positive range change feature in exactly the same location as the feature in the coseismic interferogram, the NW/SE-trending hinge line running inland from the coast is again evident, and the wavelength of the surface deformation is similar to the coseismic case. Bearing in mind that both coseismic and postseismic interferograms are overprinted by a Maule relaxation signature, the maximum magnitude of postseismic LOS surface displacement (8.4 cm) is about one sixth that for the coseismic case. It should be noted that postseismic surface displacement would have occurred during the two weeks before the first radar acquisition, and likely continued after the second acquisition.

4.3 GPS data

We include in our analysis data from three cGPS sites near Pichilemu that span the earthquakes. Site LEMU is in the town of Pichilemu, while NAVI lies about 50 km to the NNE and ILOC about 60 km to the SSW. The data are processed using the TRACK module of GAMIT/GLOBK (King & Bock, 2000; Herring et al., 2010), which uses a Kalman filtering approach to produce epoch-by-epoch time series. The events occur 90-105 km to the NW of site CURI, which means that this site is not only distant from the Pichilemu epicentres but also lies in a quadrant of minimal displacement (e.g. see Figures 3 and 7). CURI is therefore assumed to be insignificantly affected by the earthquake sequence and is used as a fixed base station. The network is augmented with three additional sites (CONS, SANT, VALP) within approximately 200 km that also show no displacement due to the aftershocks beyond the level of noise in the time series. ILOC, LEMU and NAVI are treated as "kinematic" sites and their positions solved for at 30 s intervals relative to CURI from one hour before the first to one hour after the second event (2010-03-11 13:40Z-15:55 UTC). All sites are initially constrained to a static position by allowing zero random walk process noise in the Kalman filter, but with random walk noise added to the Kalman filter for three epochs (approximately one minute) after the time of each earthquake at sites ILOC, LEMU and NAVI to allow them to move in response to the events. With integer ambiguities estimated and fixed, random walk noise of 1 m/sqrt(epoch) is included for ILOC, LEMU and NAVI throughout a final pass to allow each epoch to be essentially independent, providing a realistic estimation of noise level in the data and epoch-by-epoch positional uncertainties. The displacements due to each earthquake are then estimated as offsets in the resulting time series using points from 15 minutes before, between and after the earthquakes.

The GPS displacements and their formal errors are given in Table 1, and the displacement vectors are shown for both earthquakes in Figure 4, along with coseismic line-of-sight displacement contours from the InSAR data. Displacement at sites LEMU and ILOC show a reversal of motion in the second event relative to the first, though generally with smaller amplitude. The motion of LEMU to the SW and downward in the first event is consistent with it being in the hanging wall of a SW-dipping normal fault, as inferred from the InSAR data. A possible explanation of the reversal is that the two earthquakes ruptured the same fault, with the second event having reverse motion. However, a more likely scenario is that two different normal faults were involved, with the first dipping to the SW and a second, smaller/deeper synthetic fault to the SW of the first such that LEMU is in the hanging wall of the first event and the footwall of the second event. This is explored in detail in the modelling section below.

5. Source parameters of the Pichilemu earthquakes

5.1 General modelling methodology

Because field investigation did not yield information on fault location or geometry of the Pichilemu earthquakes, we analyse the geodetic data to constrain the source mechanism of the two events. We work in a coordinate system whose origin is the town of Pichilemu (34.402ºS,72.009ºW). For two different fault configurations, we estimate the magnitude of slip on discrete fault patches that are approximately 2.5 km long by 2.5 km down-dip. Green's functions are computed, relating unit slip on fault patches to surface displacements in a homogeneous elastic half-space (Okada, 1985). The interferogram is down-sampled according to the quadtree algorithm described by Jonsson et al. (2002), yielding 8896 points (Fig. 5). The down-sampled interferogram LOS values are weighted using an inverse covariance matrix generated from analysis of noise in the interferogram (see Appendix D for details), **augmented with the GPS displacements, and then inverted for slip using a smoothed linear least squares approach.** To allow for the longer-wavelength deformation associated with the Maule earthquake postseismic relaxation, and for satellite orbit error, we also solve for a quadratic function across the interferogram. **It is important to emphasize that the InSAR data still include 6 weeks of local postseismic deformation, in contrast to the GPS data, which represent the very rapid displacements of the Pichilemu earthquakes. The rake on individual fault patches is allowed to vary between -90 and -180, i.e. the slip direction is constrained to lie in the quadrant between pure normal and pure right-lateral, compatible with the range of rakes estimated in the Global CMT and USGS focal mechanisms. The value of shear modulus used in the elastic calculations is 36.3 GPa, from the study by Bohm et al. (2002) of seismic velocities in Chile from 36°-40°S.**

5.2 Single fault inversion

We start by solving for distributed slip on a single SW-dipping fault plane whose projected fault trace lies between the two lobes of positive range change in the interferogram. **Even though the GPS data strongly suggest a pair of synthetic faults, we start with a single fault to allow assessment of the residual field.** Slip is allowed to occur between the surface and a depth of 24 km, which is close to the depth at which the northwestern end of the fault intersects the plate interface. The strike of the fault plane is 144º, which is the strike of the SW-dipping nodal plane in the GCMT focal mechanism and which matches the linear seismicity cluster (Fig. 1b). From observation of the seismicity distribution in this area, and in particular the linear cluster, we assume that some of the coseismic displacement pattern is offshore, and set the length of the fault to be 50 km. The dip is estimated from the seismicity profile (Fig. 2) to be between 50º and 60º, so we vary the dip between these limits to find the optimal value. Initially we do not make any differentiation between the two rupture events, either in the plane used to model the slip or in the applied smoothing. Resolution tests employing a checkerboard pattern, as described in Appendix C, indicate that the InSAR data onshore can resolve features of approximate size 6x6 km onshore down to a depth of about 15 km, with the resolution degrading offshore.

The resulting slip distribution is shown in Fig. 6a and the fault parameters are listed in Table 2. The rms misfit for this solution is 11.7 mm. The slip vectors for the main slip patch have an essentially normal sense of motion (lower panel of Fig. 6a), in agreement with the GCMT focal mechanism. Fig. 7a shows the coseismic interferogram once the best-fitting quadratic function returned in the inversion has been removed, along with a synthetic interferogram generated by forward modelling the optimal slip distribution, and its associated residual. Net displacements for both events modeled at the GPS sites are shown in Fig. 8a. There is good agreement between modeled and observed GPS vectors for all three sites, and especially at LEMU. In the

InSAR residual, there is a small zone of locally high residual (up to 12 cm) at the coast on the double promontory near Pichilemu, as well as near-fault residuals of order 4-5 cm. A significant local residual at Pichilemu is unsurprising, given the different time periods covered by the InSAR and GPS data (see Section 5.1). A fundamental problem with the single fault solution is that if the fault is split into two equal segments either along strike or down dip, with smoothing applied separately to each segment to simulate the two earthquakes, then the modeled GPS vectors in no way agree with the measured vectors; most significantly, subsidence is predicted for both events, whereas the data clearly show subsidence in Event 1 and uplift in Event 2. Vectors azimuths and magnitudes are also incorrect.

5.3 Two synthetic faults

To try and match the relative motions in each of the two events separately, as well as the net displacements, we now implement a synthetic fault geometry. We retain the SW-dipping structure from the single fault inversion (now called Fault 1), and add in another SW-dipping fault (Fault 2). Placing the second fault to the SW of the first allows site LEMU to be uplifted in Event 2. The strike of Fault 1 is retained from the single fault inversion, and the strike and dip of Fault 2 are varied under the constraint that the two faults must not cross each other. The optimal location, including depth, and geometry of the second fault are found by varying parameters in response to the GPS residuals for the individual events. Resolution tests are carried out using both checkerboards and synthetic slip distributions based on bivariate Gaussian functions, which give approximately elliptical slip patterns (see Appendix C for further details). Patches of approximate dimension 6 km are resolved onshore, as for the single fault case, and patches of dimension 10 km are resolved on the onland part of the buried fault. The inversions with synthetic slip recover the known slip distribution quite well, although the model slip is not as focused as in the original pattern.

The optimal parameters for the two-fault model are listed in Table 2, and the rms misfit for this solution is 9.8 mm. The optimal slip distribution is shown in Fig. 6b and its errors in Appendix D. The second fault has a slightly steeper dip than the first, though the two structures do not converge at depth, and is buried to a depth of 8 km. The maximum slip is 2.98 m on Fault 1 and 1.82 m on Fault 2, at depths of 10-12 and 14-16 km respectively. Notably, only a small amount of slip is predicted onshore along the upper part of the discretised fault plane, consistent with field observations that suggest a lack of surface rupture. However, the small amount of shallow slip on the offshore portion of Fault 1 was evidently enough to generate a small local tsunami. The InSAR forward model and residuals are shown in Fig. 7b, and the GPS predictions in Fig. 8b. The InSAR residuals are lower than for the single fault case, although there is still a (smaller) local residual near site LEMU, again attributable to the different time windows of the InSAR and GPS data. Inverting only the InSAR data reduces this residual to almost to the level of noise in the interferogram. In addition, the positive near-fault residuals are now very much reduced. Importantly, modelling the ground motion at the GPS sites due to each rupture individually now gives a reasonable match to the GPS displacements isolated for each event (Fig. 8b). The match is very good at LEMU and moderately good at the far-field sites NAVI and ILOC. The far-field discrepancy may be a result of sub-optimal approximation of the Maule postseismic displacement field with a simple quadratic function.

6. Coulomb stress modelling

In order to determine to what extent the faults that ruptured were brought closer to failure by the Maule earthquake, we perform calculations of Coulomb stress change, resolving the shear and normal stress changes ($\Delta\tau$ and $\Delta\sigma$ respectively) resulting from the Maule rupture onto the Pichilemu fault planes. The Coulomb failure hypothesis states that faults are brought closer to or further from failure by the Coulomb stress change resulting from an event such as an earthquake. The Coulomb stress change is defined as

$$\Delta\sigma_C = \Delta\tau + \mu'\Delta\sigma$$

where μ' is the apparent friction coefficient on the fault. We assume a value for μ' of 0.4. Since shear stresses can act in any direction along a given plane, the direction in which the resolved stresses act must be specified. Hereafter, the rake direction in which the shear stress is resolved is referred to as the "Coulomb rake". The value of shear modulus used is 36.3 GPa (from Bohm et al., 2002), as for the slip inversions. To calculate the stress changes caused by the Maule earthquake, we perform an inversion of the ascending and descending ALOS PALSAR data used in Tong et al. (2010) for slip on the subduction zone interface. The general inversion methodology is similar to that described in Section 5.1 for the Pichilemu inversions; further details and the resulting slip distribution are given in Appendix B. **Initially, the distribution of $\Delta\sigma_C$ due to the Maule rupture alone is computed on both fault planes, using Coulomb rakes of -90º for both. A large variation in $\Delta\sigma_C$ is seen (Fig. 9a), with a range of 5-90 bars for Fault 1 and 7-48 bars for Fault 2. The highest stress changes occur in the lower NW parts of Fault 1, where it comes very close to the top of the subducting slab on which the February rupture occurred, but note that this is outside the zone that slipped in the first Pichilemu earthquake. The range of $\Delta\sigma_C$ over the areas that slipped is about 15-40 bars for Fault 1 and 0-35 bars for Fault 2.**

We also test how the first Pichilemu rupture would have modified the stress change on the second fault. Fig. 9b shows the net stress changes on the two fault planes due to both the Maule rupture and Pichilemu Event 1, again using Coulomb rakes of -90º. As expected, there is a large stress drop on Fault 1 itself, reflecting the slip distribution. The most highly-stressed region on Fault 2 is in the northwestern part, which is consistent with where the slip is estimated to have occurred in Event 2 (compare Fig. 6b). Finally, we calculate the stress changes caused by the two Pichilemu earthquakes on the plate interface below, using the rakes for each patch obtained in the Maule inversion as the Coulomb rake values. **A maximum stress increase of +4.5 bars occurs on the plate interface to the west of Pichilemu, with nearby patches within a radius of about 20 km having smaller positive or negative stress changes.**

7. Discussion

The majority of aftershocks following the Maule earthquake, and megathrust events in general, are located near the plate interface, and moderate to large aftershocks at the depth of the plate interface may not cause sufficiently strong ground motions to pose a hazard. However, any shallow aftershocks in the upper crust of the overriding plate may represent a significant seismic hazard because of small source-to-site distances and relatively strong ground motions in frequency ranges of concern to engineered structures. The InSAR data and seismic event locations presented in this paper clearly show that the Pichilemu earthquakes of 11 March 2010 were shallow crustal events that occurred in the overriding South American plate. Following the Maule earthquake, Coulomb stress increases up to 40 bars were induced on the parts of the Pichilemu faults that slipped. This range extends well above the threshold of 0.5-1

bars that is often cited to promote failure (e.g. King et al., 1994 and Lin and Stein, 2004), and so it is likely that the Pichilemu events were triggered by the Maule earthquake. **The strike of the Pichilemu faults (144º) and the relative plate motion are such that the angle between the normal to strike and the plate motion vector is only about 25º. In other words, the Pichilemu faults would normally be subjected to compressional stresses from the convergence of the Nazca and South American plates. However, the occurrence of large extensional earthquakes in the continental forearc of central Chile following a megathrust event suggests that the pre-earthquake regional tectonic stress is only weakly compressional. Perturbation of the background stress field by the subduction zone rupture presumably establishes a temporary tensile regime in the forearc, which will eventually become compressional again as interseismic stresses accumulate. We note that no crustal normal faulting events with M > 3 occurred in the area during the 25 years prior to the Maule earthquake.**

We consider these earthquakes to have been triggered by static stress changes from the Maule main shock, but it is not clear at this point whether these aftershocks occurred at Pichilemu primarily because there were pre-existing faults there (reverse or normal) or because the area is adjacent to the zone of maximum slip in the Maule rupture. Other shallow crustal faults in the large area stressed by the Maule earthquake may also have been brought closer to failure and may produce earthquakes in the future, with the type and size of earthquake depending on the configuration of the pre-existing fault(s) relative to the Maule stress field. Recent large shallow normal-faulting earthquakes in Japan following the 11 March, 2011 Tohoku-Oki megathrust earthquake may likewise be a direct result of triggering by the rupture on the subduction zone interface. **In their seismological study of these events in Japan, Kato et al. (2011) suggest that the stress field in the area changed from compressional to extensional as a result of the megathrust rupture, exactly analogous to the Pichilemu scenario.**

We note that the Pichilemu earthquakes of 11 March 2010 did not occur on the N-S striking Pichilemu-Vichuquén Fault (PVF), which has a left-lateral reverse sense of motion (Willner et al., 2009). This east-dipping fault formed 100 Ma years ago and represents a mid-Cretaceous shortening event, during which the accretionary Eastern Series was thrust over the structurally-underlying Western Series. The traces of the PVF and the SE-striking onshore fault described in the present study are approximately coincident where they both go offshore in the bay north of Pichilemu. The fact that the observed seismic activity has been shown to occur on the SE-striking fault, which cross-cuts the PVF, suggests that the PVF is no longer active. The two faults we infer in our analysis were not previously mapped, but may have existed prior to 2010.

The preferred slip model obtained in this study sheds light on the discrepancy between the GCMT and NEIC moment magnitudes for Event 2 (7.0 and 6.7 respectively), and therefore the relative sizes of the two Pichilemu aftershocks. In general, GCMT and W-phase M_w values show close agreement for earthquakes globally, with a maximum variation of about 0.3 (Hayes et al. 2009), which is the variation encountered here for Event 2. The two-fault model gives moment release values of 3.17 x 10^{19} and 1.54 x 10^{19} N m for Events 1 and 2 respectively, which are equivalent to moment magnitudes of 6.97 and 6.76. These geodetic magnitudes are more in line with the NEIC values of 6.9 and 6.7 than with the GCMT values of 6.9 and 7.0. The smaller GPS displacements for Event 2 also suggest that this was the smaller of the two earthquakes (notwithstanding the fact that the fault was buried, which would also lead to smaller surface motion). The GCMT focal mechanism for Event 2 may have been compromised by the moment/dip trade-off first highlighted by Kanamori and Given (1981) for shallow dip-slip earthquakes.

The higher moment inferred from the fault slip pattern relative to the NEIC moments may be explained by slip occurring aseismically after the two earthquakes. This is consistent with the observation of post-aftershock deformation in the March 26 – June 4 Envisat interferogram. There is close similarity between the aftershock (Fig. 3a) and post-aftershock (Fig. 3b) interferograms (despite the different satellites and viewing geometries), in particular the lobe of positive range change on the southwestern side of the fault trace. This repeated feature indicates that part of the fault plane that slipped during the two aftershocks continued to slip aseismically during some or all of the time covered by the post-aftershock interferogram. Close similarity of coseismic and postseismic surface displacement patterns was also observed in the case of the 2008 M_w 6.4 Nima-Gaize earthquake in Tibet (Ryder et al., 2010), where near-pure normal faulting on two faults in synthetic configuration was followed by aseismic slip on both structures. As for the Nima-Gaize case, it is likely that afterslip at Pichilemu commenced immediately following the aftershocks, and continued at diminishing rates after the InSAR observation period.

Northeast of the fault trace (near 34.1ºS), there is another lobe of positive LOS change in the postseismic image (see Fig. 3b) that is not present in the coseismic image, and which is not predicted by projecting the aftershock forward model surface displacement components into the Envisat descending line-of-sight. It is possible that this feature is an artifact resulting from the presence of tropospheric water vapour. Two other Envisat interferograms were produced (2010/03/26-2010/04/30 and 2010/04/30-2010/06/04) to try and establish whether this is the case (Appendix A). The acquisition on 30 April 2010 is clearly heavily affected by tropospheric water vapour, since broad-scale phase features across the image flip sign between these two additional interferograms. In contrast, the unexplained coastal phase feature is only evident in the earlier interferogram, where a diffuse zone of positive range change is seen at the coast. However, this zone joins up with what is inferred to be an atmospheric signature to the north. No pairs of ALOS PALSAR scenes had low enough orbital baselines to enable postseismic interferograms to be constructed. At this point it is therefore unclear exactly what this phase feature is. While it may be a result of tropospheric water vapour, it may represent aseismic tectonic motion activated after, and perhaps by, the aftershocks and/or the subsequent afterslip, and may be related to the seismicity ~30 km offshore (Fig. 1b). First-order model exploration suggests that a large aseismic slip transient on the plate interface can produce the observed feature. The transient would involve up to 2.8 metres of slip between depths of about 10 and 20 km, in a zone which lies beneath the trench-parallel seismicity cluster offshore (34ºS,72.4ºW) seen in Fig. 1b. Since the Pichilemu events gave rise to a stress increase of up to 4.5 bars on the plate interface offshore, it is possible that enhanced seismic activity will occur on or near the interface in the future, but it is not possible to make any statement about the timing of such activity.

8. Conclusions

In this paper we investigate the pair of large earthquakes that occurred within 15 minutes of each other on 11 March 2010 near the town of Pichilemu, central Chile, two weeks after the M_w 8.8 Maule earthquake. InSAR data and aftershock seismicity provide a means to locate the faults and estimate source parameters for these events. According to our preferred model, the ruptures occurred on a pair of faults in synthetic configuration dipping to the SW. The first fault extends from the surface down to about 22 km and the second fault is buried, extending from a depth of 8 km to 20 km. The sense of motion on the first fault is largely pure normal, while the rake is more oblique on the second fault, including some dextral strike slip. In the weeks following the two earthquakes, aseismic afterslip is inferred to have occurred on the same two faults. Both faults were brought closer to failure by the February 2010 Maule earthquake, with **positive Coulomb stress changes in the range 0-40 bars**. We therefore consider these

earthquakes to be large aftershocks of the February 2010 Maule megathrust earthquake. **The occurrence of extensional ruptures in a zone of interseismic compression means that the background compressional stress must be low, and as interseismic convergence proceeds following the Maule earthquake, we expect that a compressional regime will eventually be re-established.** It is possible that other pre-existing (and possibly unknown) shallow faults in the large area affected by the Maule rupture have been brought closer to failure, in which case they potentially represent a significant seismic hazard. The Pichilemu aftershocks may be an analogue for several shallow normal faulting earthquakes that have occurred recently following the M_w9.0 Tohoku-Oki megathrust earthquake in Japan.

Acknowledgements

SAR data were obtained via the Chile Supersite initiative, and we are grateful to IRIS, IPGP, ENS and GFZ for making their seismic data available. We thank Christian Ledezma and Nicholas Sitar for field collaboration, and Kelson thanks GEER and Fugro William Lettis & Associates for support of field investigations. The manuscript benefitted from useful discussions with Sierra Boyd, Diana Comte, Steven Roecker, Mong-Han Huang, Fred Pollitz and Gavin Hayes, and from review by Ross Stein. Thanks to Xiaopeng Tong et al. for making available their reduced ALOS PALSAR data for the Maule earthquake.

References

Antonioli, A., Piccinini, D., Chiaraluce, L. and Cocco, M. (2005), Fluid flow and seismicity pattern: Evidence from the 1997 Umbria Marche (central Italy) seismic sequence, *GRL,* **32**, L10311.

Bohm, M., Lüth, S., Echtíer, H., Asch, G., Bataille, K., Bruhn, C., Rietbrock, A. and Wigger, P. (2002), The Southern Andes between 36 and 40°S latitude: seismicity and average seismic velocities, *Tectonophysics*, **356**, 275–289.

Delouis, B., Nocquet, J. M. and Vallée, M. (2010), Slip distribution of the February 27, 2010 Mw=8.8 Maule Earthquake, central Chile, from static and high-rate GPS, InSAR, and broadband teleseismic data, *GRL*, L17305.

Flueh, E.R., N. Vidal, C.R. Ranero, A. Hojka, R. von Huene, J. Bialas, K. Hinz, D. Cordoba, J.J. Danobeitia and C. Zelt (1998), Seismic investigation of the continental margin off- and onshore Valparaiso, Chile, *Tectonophysics*, **288**, 251-263.

Hayes, G., Rivera, L. and H. Kanamori (2009), Source Inversion of the W-Phase: Real-time Implementation and Extension to Low Magnitudes, *Bull. Seismol. Soc. Am.*, **80(5)**, 817-822.

Heinze, B. (2003), Active Intraplate Faulting in the Forearc of North Central Chile (30°-31°S), *PhD thesis,* Freien Universität Berlin.

Herring, T.A., King, R.W. and McClusky, S.C. (2010), Introduction to GAMIT/GLOBK Release 10.4, http://www-gpsg.mit.edu/~simon/gtgk/index.html.

Ito, Y. and Obara, K. (2006), Dynamic deformation of the accretionary prism excites very low frequency earthquakes, *GRL*, **33**, L02311.

Ito, Y., Y. Asano and K. Obara (2009), Very low-frequency earthquakes indicate a transpressional stress regime in the Nankai accretionary prism, *Geophys. Res. Lett.*, **36(20)**, L20309.

Jackson, J. and White, N. (1989), Normal faulting in the upper continental crust: observations from regions of active extension, *J. Struc. Geol.*, **11(1/2)**, 15-36.

Jonsson, S., H. Zebker, P. Segall and F. Amelung (2002), Fault slip distribution of the 1999 *Mw* 7.1 Hector Mine, California, earthquake, estimated from satellite radar and GPS measurements, *Bull. Seismol. Soc. Am.*, **92**, 1377–1389.

Kanamori, H. & Given, J. W. (1981), Use of long-period surface waves for rapid determination of earthquake-source parameters, *Phys. Earth Planet. Inter*., **27**, 8–31.

Kato, A., Sakai, S. and Obara, K. (2011), A normal-faulting seismic sequence triggered by the 2011 off the Pacific coast of Tohoku Earthquake: Wholesale stress regime changes in the upper plate, Earth, Planets and Space, **63**, 745-748.

Khazaradze, G. and Klotz, J. (2003), Short and long-term effects of GPS measured crustal deformation rates along the South-Central Andes, *JGR*, **108(B4)**, 1-13.

King, R.W. & Bock, Y. (2000), Documentation for the GAMIT GPS Software Analysis Version 9.9, 365 Mass. Inst. of Technol., Cambridge.

King, G.C.P., Stein, R.S. and Lin, J. (1994), Static Stress Changes and the Triggering of Earthquakes, *BSSA*, **84(3)**, 935-953.

Lay, T., C. J. Ammon, H. Kanamori, K. D. Koper, O. Sufri and A. R. Hutko (2010), Teleseismic inversion for rupture process of the 27 February 2010 Chile (Mw 8.8) earthquake, *GRL*, **37**, L13301.

Lin, J. and Stein, R.S. (2004), Stress triggering in thrust and subduction earthquakes and stress interaction between the southern San Andreas and nearby thrust and strike-slip faults, *JGR,* **109**, B02303.

Lorito, S., F. Romano, S. Atzori, X. Tong, A. Avallone, J. McCloskey, M. Cocco, E. Boschi and A. Piatanesi (2011), Limited overlap between the seismic gap and coseismic slip of the great 2010 Chile earthquake, *Nature Geoscience,* doi:10.1038/ngeo1073.

Moreno, M., Rosenau, M., Oncken, O. (2010), 2010 Maule earthquake slip correlates with pre-seismic locking of Andean subduction zone, *Nature*, **467**, 198-202.

Obara, K. and Y. Ito (2005), Very low frequency earthquakes excited by the 2004 off the Kii peninsula earthquakes: A dynamic deformation process in the large accretionary prism, *Earth Planets and Space*, **57**, 321-326.

Okada, Y. (1985), Surface deformation due to shear and tensile faults in a half-space, *Bull. Seismol. Soc. Am.*, **75(4)**, 1135–1154.

Okada, Y., K. Kasahara, S. Hori, K. Obara, S. Sekiguchi, H. Fujiwara and A. Yamamoto (2004), Recent progress of seismic observation networks in Japan—Hi-net, F-net, K-NET and KiK-net, *Earth Planets and Space*, **56**, 15-28.

Pollitz, F., Brooks, B., Tong, X., Bevis, M.G., Foster, J.H., Burgmann, R., Smalley Jr., Vigny, C., Socquet, A., Ruegg, J.-C., Campos, J., Barrientos, S., Parra, H., Baez Soto, J.C., Cimbaro, S., Blanco, M. (2011), Coseismic slip distribution of the February 27, 2010 Mw 8.8 Maule, Chile earthquake, *GRL*, **38**, L09309.

Rietbrock, A., Ryder, I., Haberland, C., Nippress, S., Agurto, H., Barrientos, S., Bataille, K., Beck, S., Bernard, P., Campos, J., Comte, D., Heit, B., Lange, D., Miller, M., Peyrat, S., Roecker, S., Schurr, B., Tilmann, F. and J.-P. Vilotte (2010), Aftershock Seismicity of the Mw 8.8 Maule Earthquake of 27 February 2010 using a 2D Velocity Model, *American Geophysical Union Fall Meeting 2010,* Abstract #G33A-0819.

Ruegg, J. C., A. Rudloff, C. Vigny, R. Madariaga, J.B. de Chabalier, J. Campos, E. Kausel, S. Barrientos and D. Dimitrov (2009), Interseismic strain accumulation measured by GPS in the seismic gap between Constitución and Concepción in Chile, *Physics of the Earth and Planetary Interiors*, **175**, 78-85.

Ryder, I., Bürgmann, R. and Sun, J. (2010), Tandem afterslip on connected fault planes following the 2008 Nima-Gaize (Tibet) earthquake: *J. Geophys. Res.*, **115(B3)**, doi:10.1029/2009JB006423.

Tong, X., D. Sandwell, K. Luttrell, B. Brooks, M. Bevis, M. Shimada, J. Foster, R. Smalley Jr., H. Parra, J. C. Báez Soto, M. Blanco, E. Kendrick, J. Genrich and D. J. Caccamise II (2010), The 2010 Maule, Chile earthquake: Downdip rupture limit revealed by space geodesy, *GRL*, **37**, L24311.

Vigny, C., Socquet, A., et al. (2011) The 2010 Mw 8.8 Maule Mega-Thrust Earthquake of Central Chile, Monitored by GPS, *Sciencexpress,* 10.1126/science.1204132.

Von Huene, R., J. Corvalan, E.R. Flueh, K. Hinz, J. Korstgard, C.R. Ranero and C. S. W. Weinrebe (1997), Tectonic control of the subducting Juan Fernandez Ridge on the Andean margin near Valparaiso, Chile, *Tectonics*, **16(3)**, 474-488.

Weston, J. M., Ferreira, A. M. and Funning, G. J. (2010) Global Compilation of InSAR Earthquake Source Models: Comparisons with Seismic Catalogues and the Effects of 3D Earth Structure, *American Geophysical Union Fall Meeting 2010*, Abstract #G12A-08.

Williams, S.D.P. (2008), GPS coordinate time series analysis software, *GPS Solutions*, **12**, 147-153.

Willner, A.P., Richter, K. and Ring, U. (2009), Structural overprint of a late Paleozoic accretionary system in north-central Chile (34°-35°S) during post-accretional deformation, *Andean Geology*, **36(1)**, 17-36.

Table 1. Displacements measured at three cGPS sites within the study area.

Site	Event	East (mm)	East error (mm)	North (mm)	North error (mm)	Up (mm)	Up error (mm)
NAVI	**Event 1**	7.52	3.52	15.00	4.12	-12.72	9.69
	Event 2	6.11	3.68	10.73	3.87	2.70	10.99
LEMU	**Event 1**	-150.08	3.49	-72.14	4.08	-562.03	9.63
	Event 2	58.97	3.66	14.23	3.84	106.15	10.88
ILOC	**Event 1**	-3.44	3.53	-18.84	4.55	15.26	10.41
	Event 2	-4.00	3.64	18.67	3.80	-65.59	10.72

Table 2. Source parameters of the Pichilemu earthquakes, according to the Global CMT and NEIC catalogues and the two models presented in this paper. Latitude and longitude refer to the centroid location for the GCMT and NEIC entries and the centre of the fault trace for the InSAR-derived models. Depth refers to centroid depth for the GCMT and NEIC entries.

[a] USGS surface wave CMT solution

[b] USGS W-phase CMT solution

	Latitude	Longitude	Length (km)	strike	dip	rake	Depth (km)	Moment (Nm)	M_w
Global CMT									
Event 1	-34.54	-72.11	-	144	55	-90	12.9	2.39×10^{19}	6.9
				324	35	-90			
Event 2	-34.53	-72.13	-	159	86	-93	16.3	3.49×10^{19}	7.0
				16	6	-53			
NEIC									
Event 1	-34.29	-71.89	-	-	-	-	11	-	6.9[a]
Event 2	-34.33	-71.80	-	-	-	-	18	-	6.7[b]
Single fault	-34.40	-71.92	50	144	53	Fig. 6a	0-25	4.23×10^{19}	7.05
Two faults									
Fault 1	-34.40	-71.92	40	144	53	Fig. 6b	0-22	3.17×10^{19}	6.97
Fault 2	-34.43	-72.03	40	144	60	Fig. 6b	8-20	1.54×10^{19}	6.79

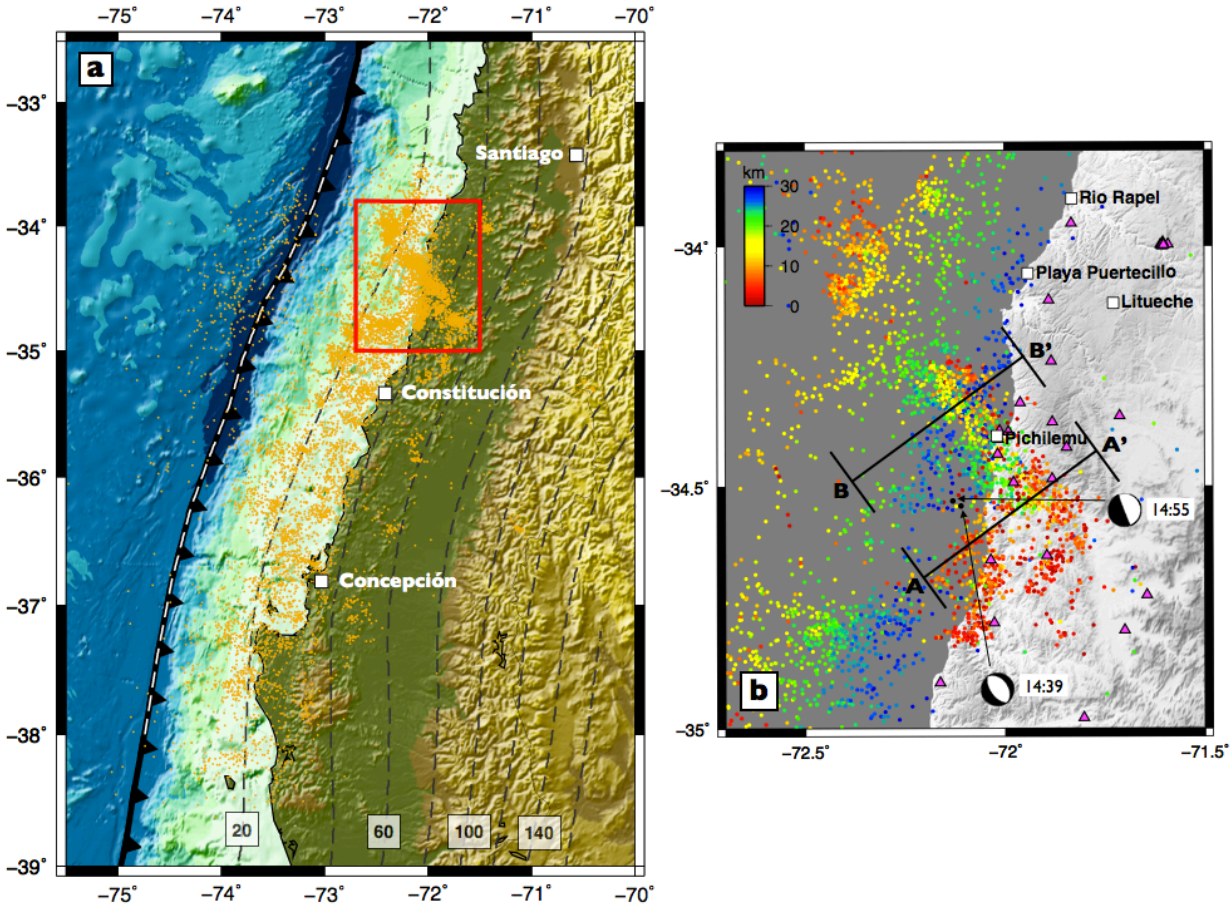

Figure 1. (a) Location map showing the extent of the February 2010 Maule earthquake rupture (white dotted line at trench), Slab1.0 plate interface contours from the USGS (grey dotted lines) and aftershock seismicity between 20 March and 2 June 2010 (orange dots). The area of the Pichilemu study is outlined with a red box. (b) Zoom of the Pichilemu area. Purple triangles denote seismic stations of the IMAD network, and dots show seismicity coloured by depth. Lines A-A' and B-B' mark location of seismicity cross-section shown in Fig. 2. GCMT focal mechanisms for the two events on 11 March 2010 are shown, with the event time in GMT given next to each mechanism, and small black dots marking their locations. Large black dots mark epicentres estimated by Farias et al. (2011).

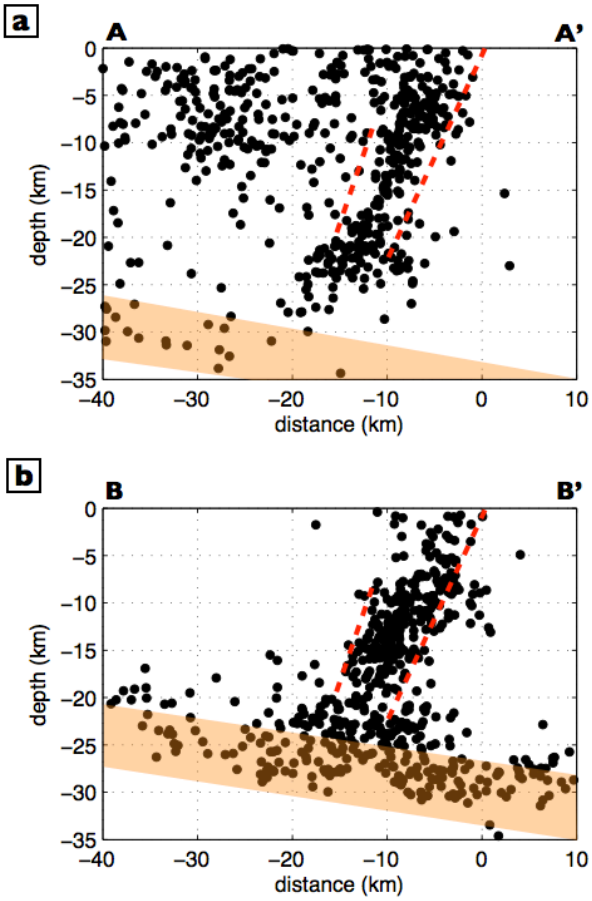

Fig. 2. Seismicity profiles along the lines shown in Fig. 1b, including events from within 10 km either side of the lines. In both (a) and (b), a SW-dipping structure is defined by the seismicity. **Red dashed lines show faults of the model obtained in this study and orange bands highlight seismicity in the downgoing Nazca plate.**

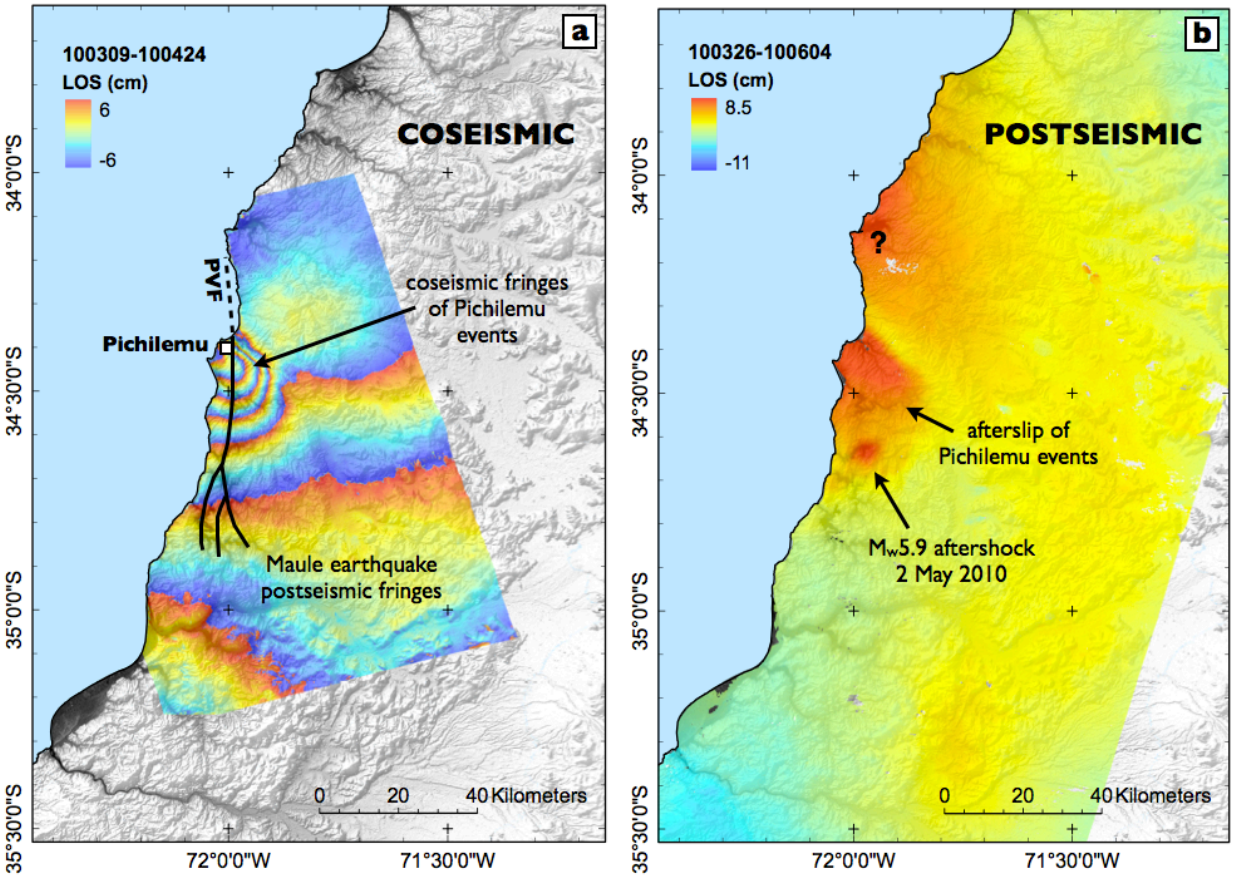

Figure 3. Interferograms for the March 2010 Pichilemu earthquakes. Acquisition dates are given in yymmdd format at the top left of each image. (a) ALOS PALSAR wrapped coseismic interferogram (ascending Track 114) covering the two aftershocks which occurred on 11 March within 15 minutes of each other, plus the first seven postseismic weeks. PVF = Pichilmeu-Vichuquén Fault. (b) Unwrapped postseismic Envisat interferogram (descending Track 53).

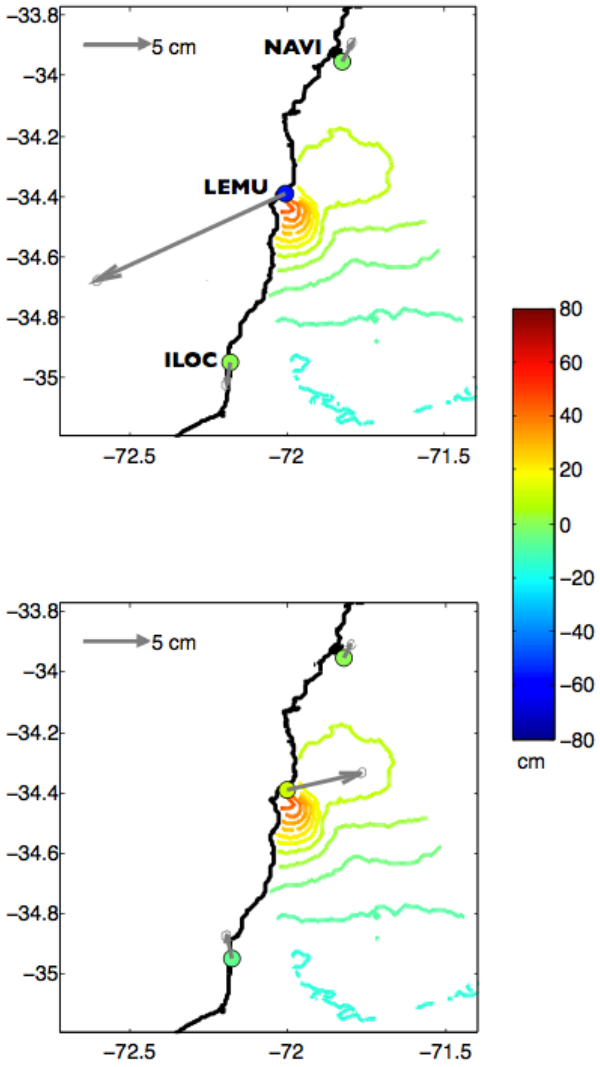

Figure 4. GPS displacements at sites NAVI, LEMU and ILOC for the two Pichilemu earthquakes. Grey arrows show horizontal displacements and coloured circles show vertical motion. Contours are line-of-sight displacements from the unwrapped coseismic interferogram.

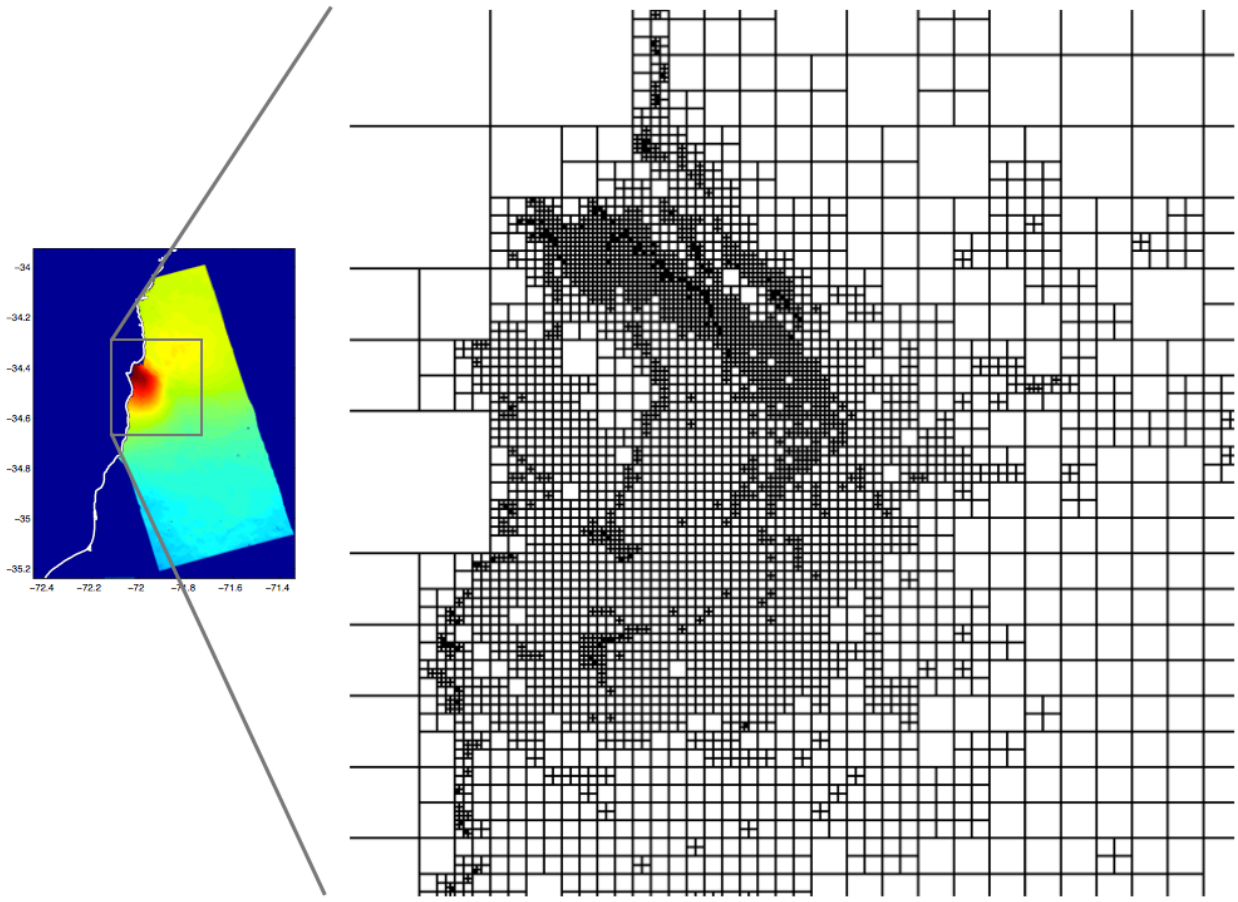

Figure 5. Part of the quadtree decomposition of the unwrapped PALSAR coseismic interferogram (shown left). The decomposition is carried out on the original unflattened interferogram.

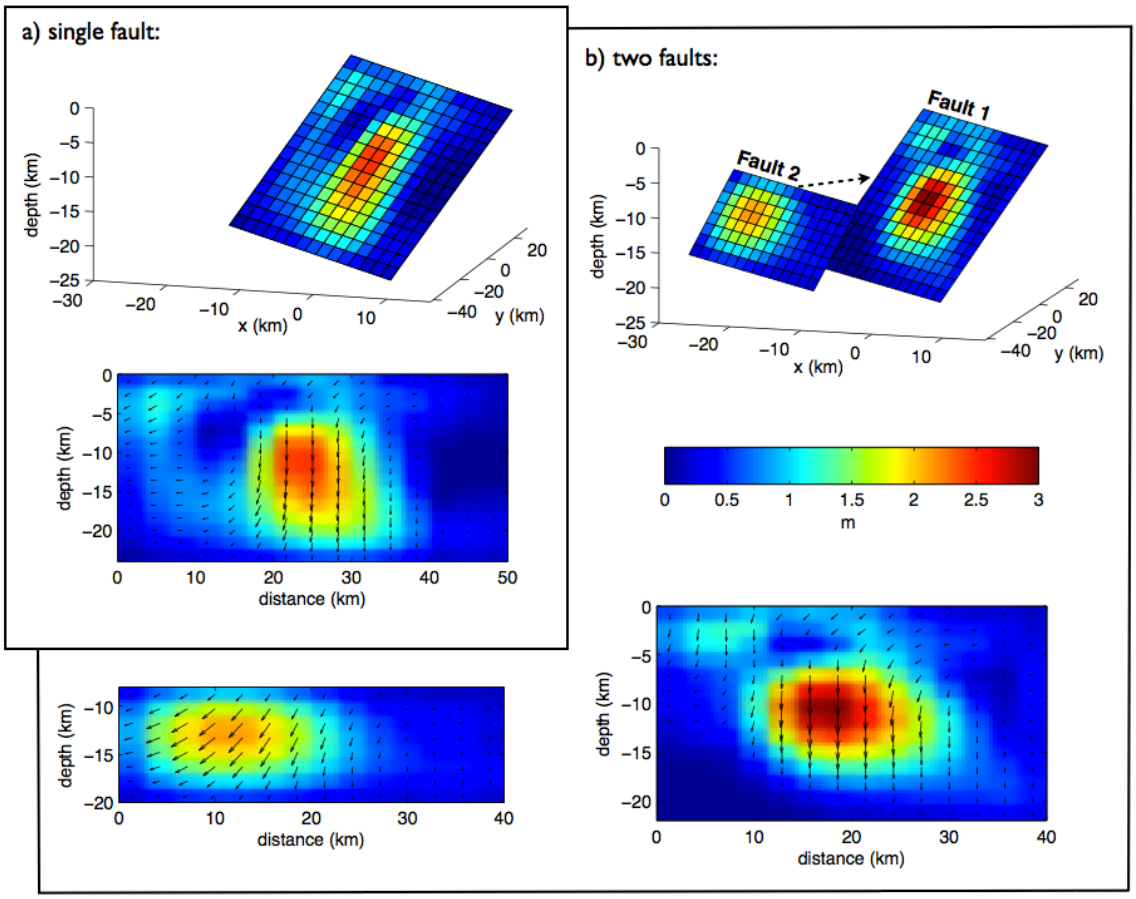

Figure 6. Slip models obtained in the distributed slip inversions. (a) Single fault model. (b) Two fault model. For clarity, Fault 2 is shown displaced a few kilometres from its actual position, as indicated by the black dashed arrow.

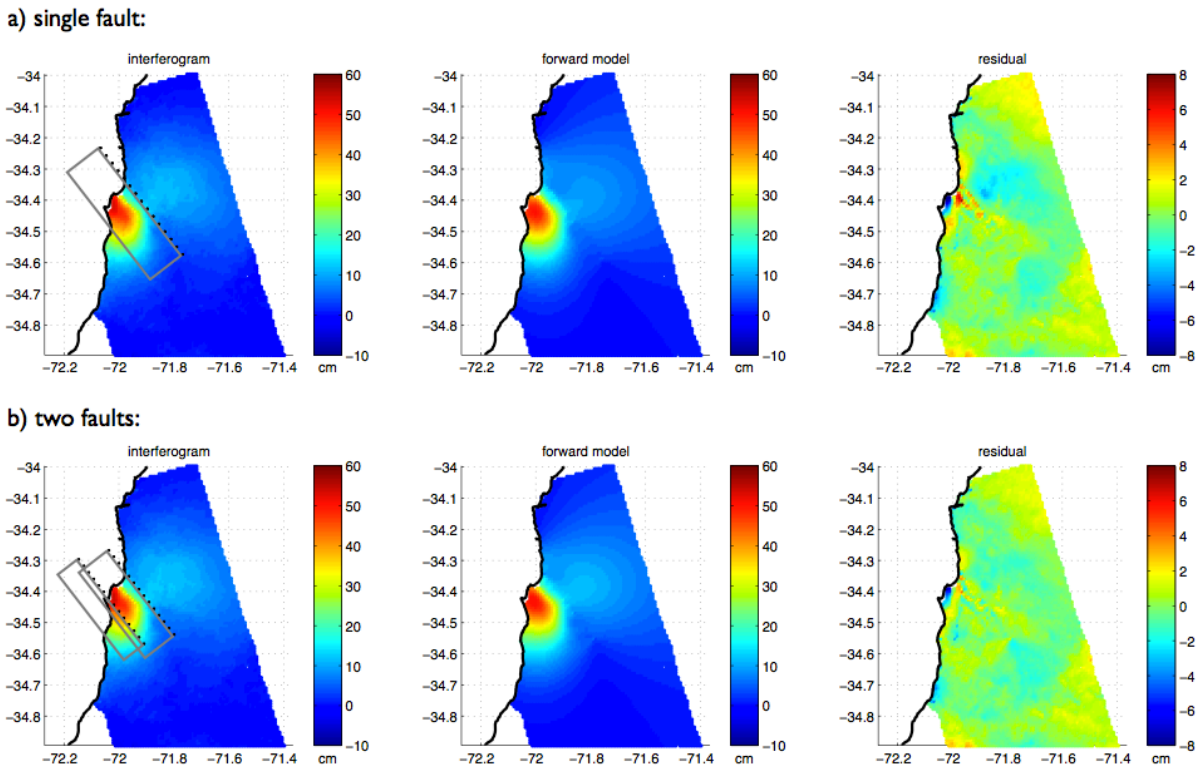

Figure 7. Surface line of sight displacements over the InSAR area, for the one and two-fault models. On the left is the original interferogram inverted to obtain the slip distributions shown in Fig. 6. Grey boxes show fault perimeters projected to the surface, with the black dotted lines marking the fault traces. Surface displacements forward modelled from the slip distributions are shown in the central column, and the associated residuals in the right hand column.

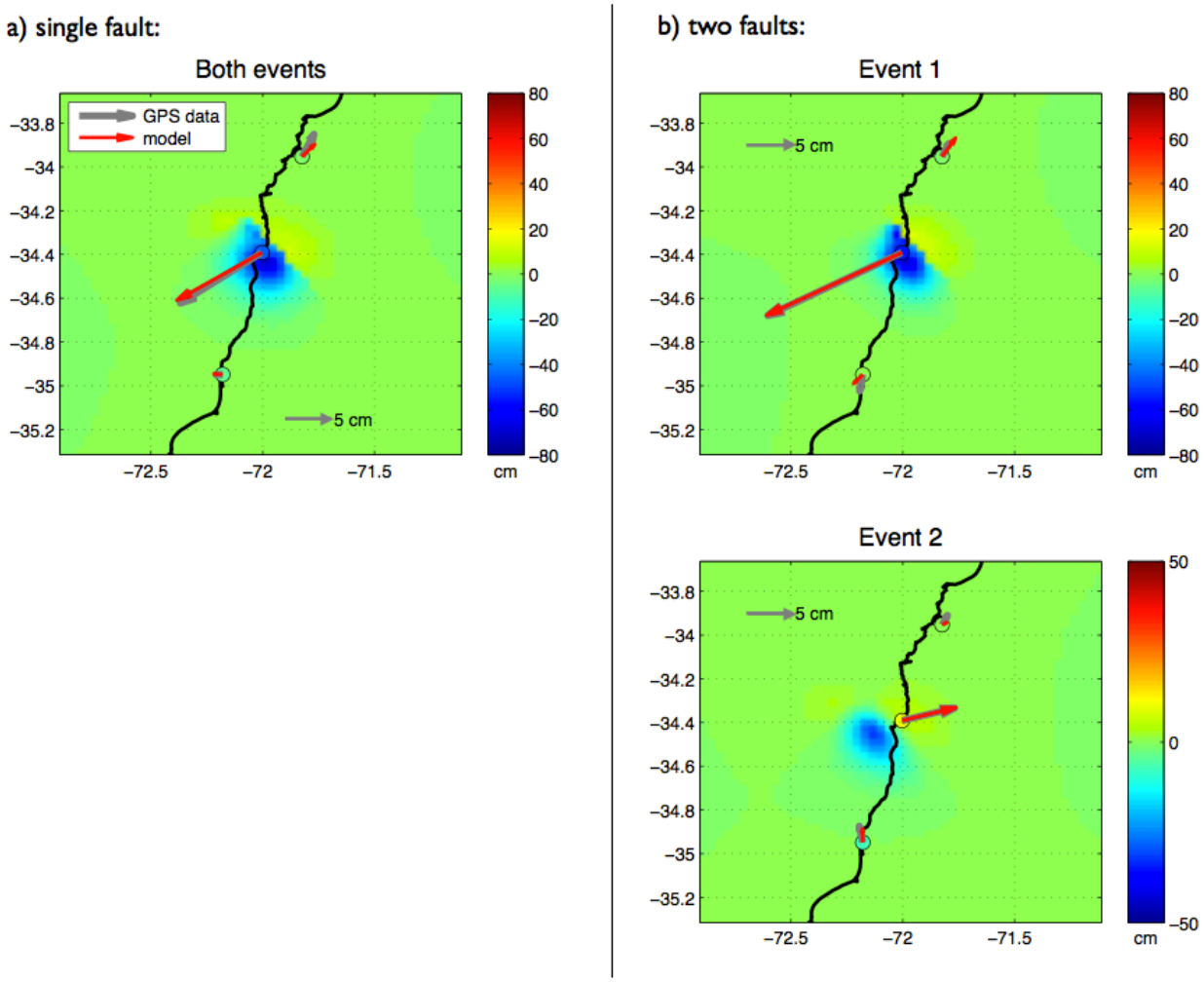

Figure 8. GPS horizontal displacement vectors (grey) along with vectors modelled from the slip distributions in Fig. 6 (red). Coloured circles are observed vertical displacements and background colour field is modelled vertical displacements. Note that although the modelled displacements in the single fault model match the observations well for both events combined, there is no way of sub-dividing the slip on this fault between the two events to give the motions observed in each event individually.

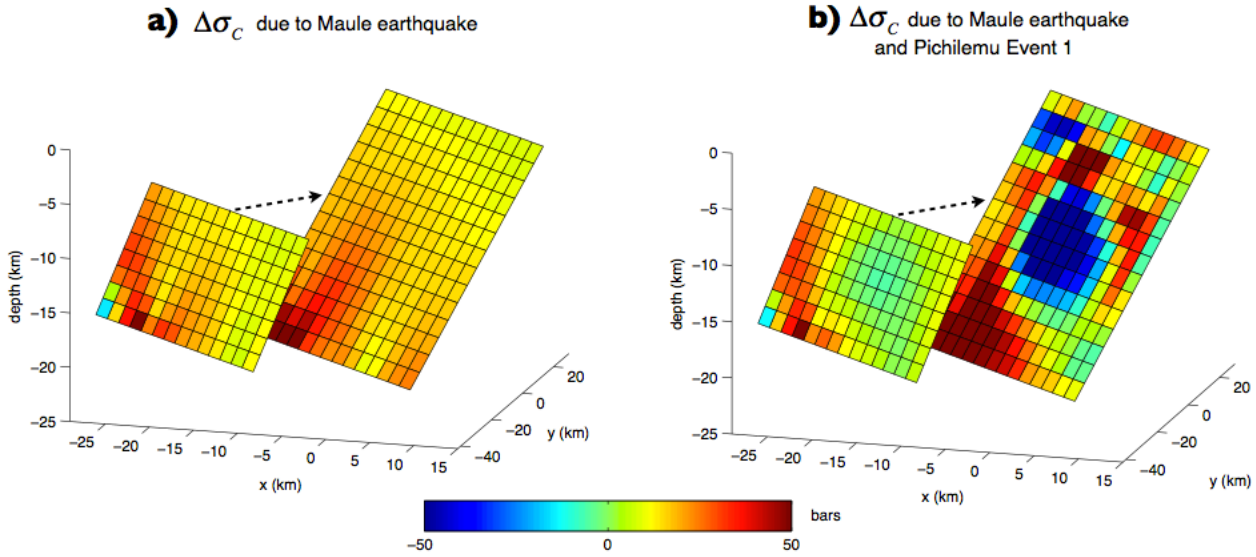

Figure 9. Coulomb stress changes resolved onto the two faults obtained from the geodetic modelling, for Coulomb rakes of -90°. (a) Stress changes due to the Maule earthquake. (b) Stress changes due to both the Maule earthquake and Pichilemu Event 1. For clarity, Fault 2 is shown displaced a few kilometres from its actual position, as indicated by the black dashed arrows.

Appendix A: Additional interferograms

Here we show three further interferograms referred to in the main text but not used in the quantitative analysis: (1) ALOS PALSAR interferogram (Track 114) covering the coseismic phase of both the Maule earthquake and the Pichilemu aftershocks; (2) Envisat interferogram (Track 53) covering one month during the postseismic phase of the Pichilemu events; (3) Envisat interferogram (Track 53) covering 9 weeks during the postseismic phase of the Pichilemu events.

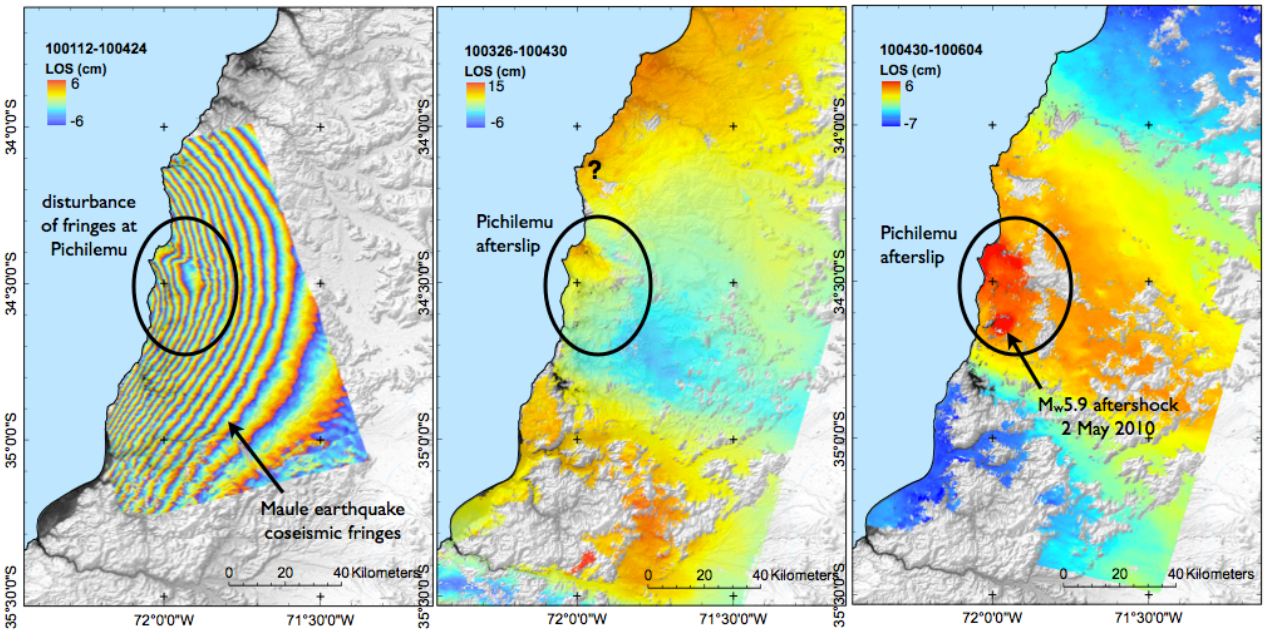

Figure A1. Additional interferograms referred to in the main text. Dates are given in the top left of each image in yymmdd format. Black circles outline the area of the Pichilemu aftershocks.

Appendix B: Maule earthquake slip distribution

In order to evaluate the stress field in the vicinity of Pichilemu caused by the Maule earthquake, we use the coseismic ALOS PALSAR dataset of Tong et al. (2010) processed using GMTSAR (http://topex.ucsd.edu/gmtsar/) and made freely available as a down-sampled, line-of-sight (LOS) dataset. We estimate the slip distribution on the subduction zone interface, assuming a planar fault with geometry as in Tong et al. (2010). To estimate the slip distribution, the fault is divided into 40 patches along strike and 10 patches down dip, and Green's functions are computed, i.e., surface displacement components on a regular grid due to 1 metre of slip on each patch. The magnitude and rake of slip on each patch are then estimated by standard least squares inversion, applying Laplacian smoothing to limit the roughness of the slip distribution. The resulting slip pattern is shown in Fig. B1. Our results are very similar to that of Tong et al. (2010), with a maximum slip of 16.1 metres at a latitude of about 35°S.

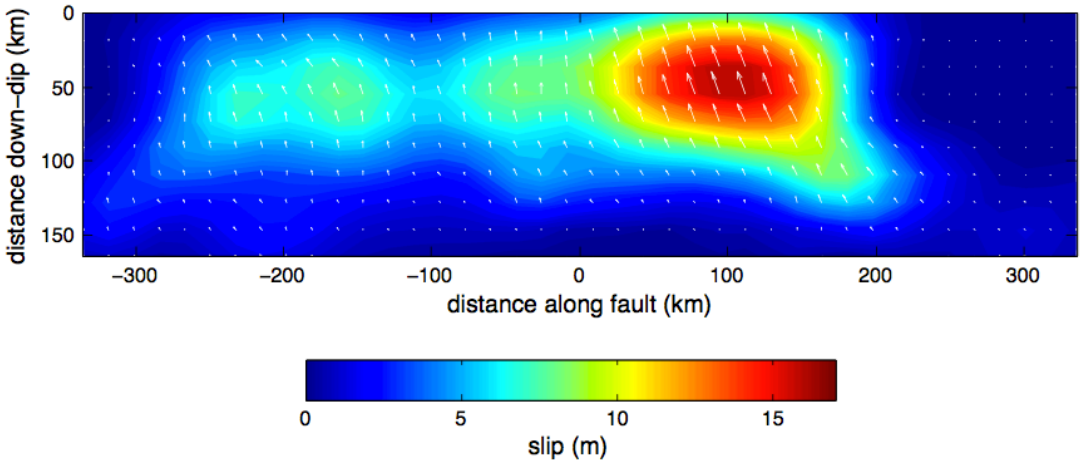

Figure B1. Slip distribution estimated from inversion of the Tong et al. (2010) ALOS PALSAR dataset. White arrows represent the slip vector on each patch.

Appendix C: Resolution tests

To test how well the InSAR data can resolve slip on the fault plane(s) in the inversions, we set up two types of tests: checkerboard and Gaussian tests. The checkerboard test was carried out for both the one and two fault scenarios, and a uniform rake of -90º was used. Checkers with slip values 0 and 2 m were assigned across the faults, and the checkered slip patterns were used to generate synthetic interferograms. Realistic correlated noise parameterised from the PALSAR interferogram as described in Appendix D was added to to the synthetic observations, and the inversion carried out in the same way described in Section 5.1. The fault patches used in the real inversion were retained, but the dimensions of the checkers were increased from 2.5x2.5 km until a reasonable recovery was achieved (Fig. C1). The lower two rows of Fig. C1 show the recovered slip for the two-fault scenario, for two different smoothing factors (κ). The higher value of κ (250) is that used in the actual InSAR inversion, while the lower value (150) is included to give a sense of how decreasing the smoothing factor focuses the returned slip. It can be seen from the figure that slip patches of approximate dimension 6x5 km can be resolved onshore down to a depth of about 15 km, and offshore the dimensions are ~10x11 km.

For the two-fault scenario, an additional resolution test was carried out. Despite multiple studies of seismic slip, it is currently not well established just how rough earthquake slip distributions really are. Since the checkerboard test shows how well oscillatory slip patterns can be recovered, for completeness we also test how well synthetic quasi-elliptical slip patterns are recovered. For this, we generate 2D Gaussian distributions by specifying the mean in the x and y directions to control the position of the centre of the slip pattern, and also a covariance matrix where the diagonal components control the spread of the slip distribution and the off-diagonal components skew the distribution away from the x and y axes. Different parameters were applied arbitrarily for the two faults, resulting in the quasi-elliptical slip distributions shown in the top row of Fig. C2. A constant scaling factor is also applied such that the maximum slip on both faults is about 4 m. The recovered slip is shown for smoothing value2 of 150 and 250. As with the checkerboard tests, the returned slip is a de-focused version of the original.

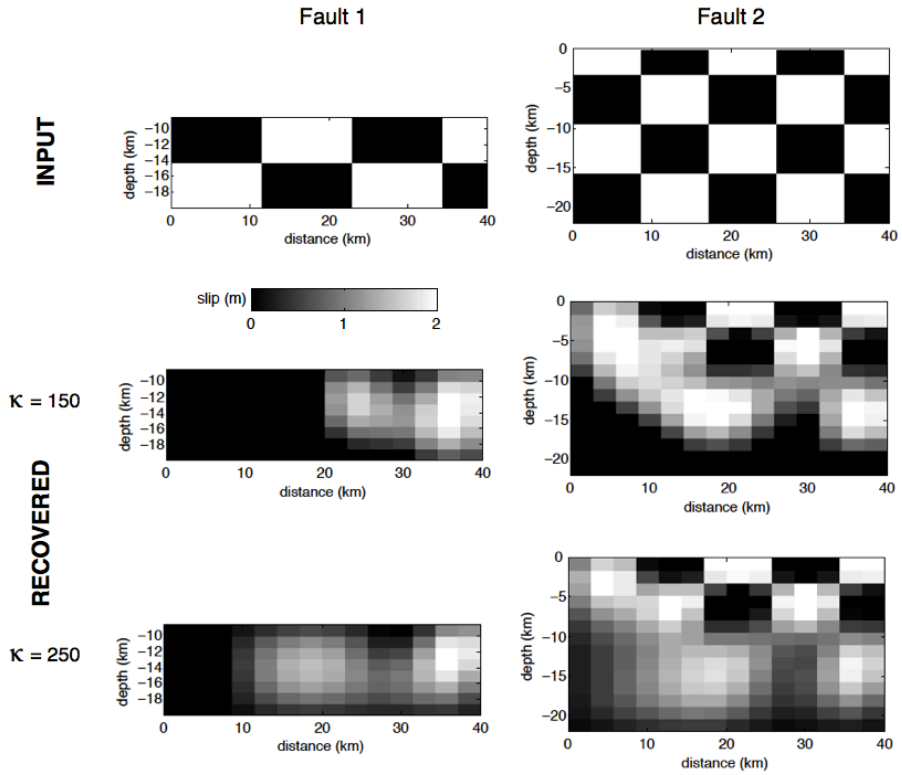

Figure C1. Results of checkerboard resolution test for the two-fault scenario. Upper panels show input slip pattern and lower two panels show the returned pattern for smoothing values (κ) of 150 and 250.

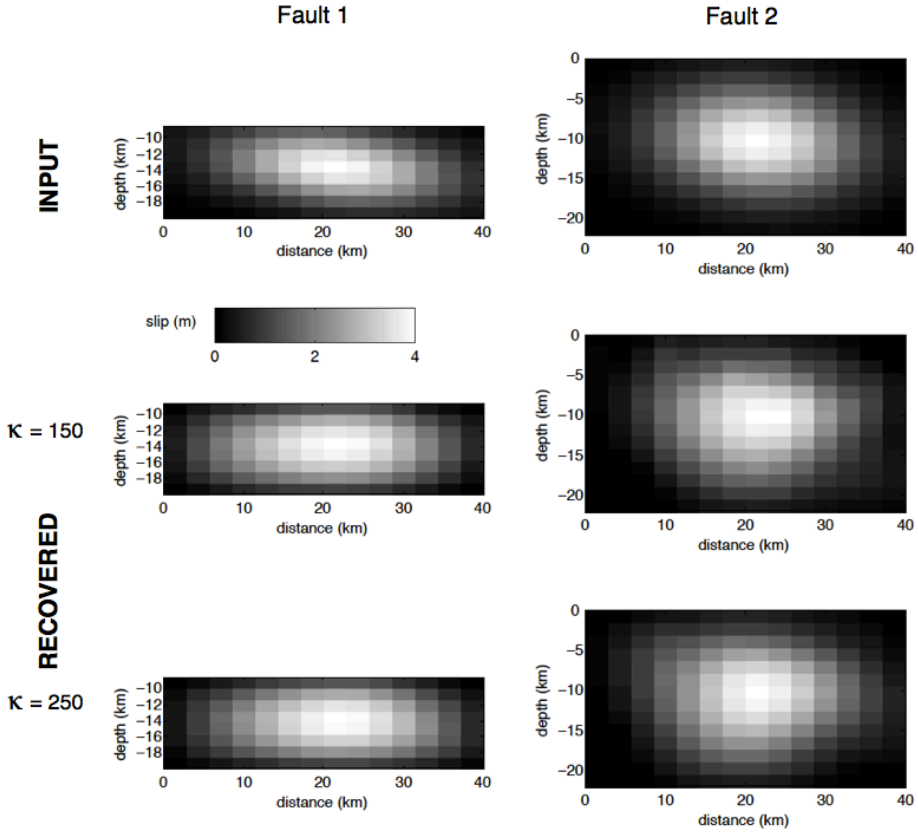

Figure C2. Results of the Gaussian resolution test for the two-fault scenario (see Fig. 6b for 3D fault geometry).

Appendix D: Spatially-correlated noise

Here we quantitatively characterise the spatially correlated noise in the PALSAR interferogram. The resulting parameters are used in several ways:

i. To weight the data vector in the least squares inversion
ii. To enable realistic noise to be added to the synthetic line-of-sight observations in the resolution tests
iii. To enable estimates of errors in the derived slip distributions using a Monte Carlo approach.

First of all it is necessary to isolate a non-deforming portion of the interferogram. Since the original interferogram is everywhere "contaminated" by postseismic deformation associated with the Maule earthquake, we first run the data inversion with no covariance weighting, solving for a quadratic function across the interferogram in addition to distributed slip. This quadratic function is removed from the interferogram, and then the southern, non-deforming portion is isolated for the noise analysis. A 2D autocorrelation grid is computed from this portion, and a radial average profile is derived from this grid (Fig. D1a). A function of the form $Ae^{-r/\rho}$ is fitted to the radial profile, where A is the maximum covariance and ρ is a length constant describing how covariance changes with distance r. These parameters are then used to generate a variance-covariance matrix to weight the InSAR data and to simulate realistic noise (e.g. Fig. D1b). The parameters obtained in the autocorrelation analysis are: A = 0.87 cm^2, ρ = 2.5 km. To estimate the errors in the derived slip distributions, 100 sets of correlated nosie are added to the downsampled interferogram before inverting, and the slip error on each fault patch is the standard deviation of the resulting slip populations for each patch (Fig. D2). As expected, the estimated errors are larger for the offshore parts of the fault(s).

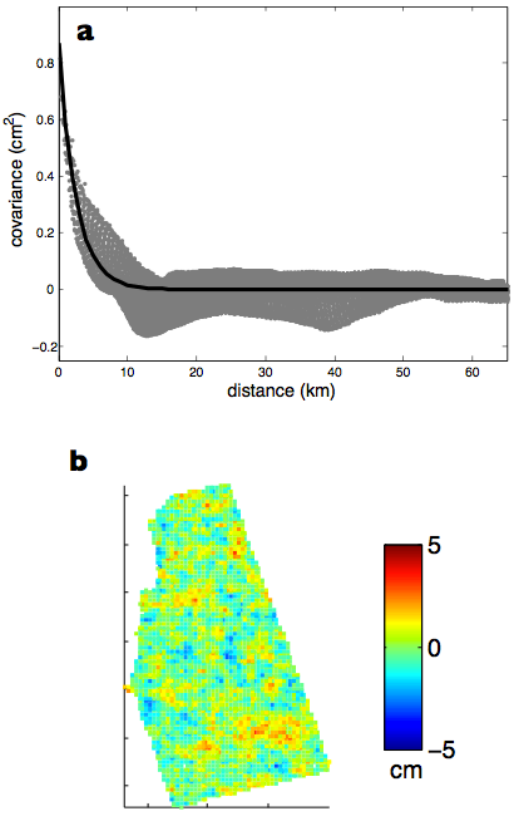

Figure D1. (a) Radial covariance profile and best-fit decaying exponential function derived from autocorrelation analysis of the flattened, non-deforming part of the coseismic PALSAR interferogram. (b) Example of spatially correlated noise generated from the autocorrelation parameters.

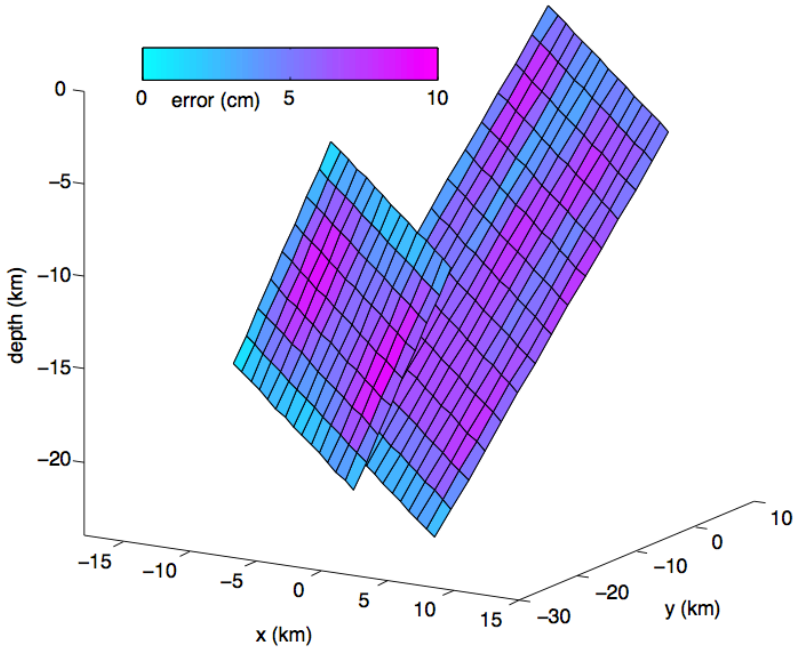

Figure D2. Errors on the two-fault slip distribution estimated from Monte Carlo analysis using 100 sets of simulated spatially correlated noise.